

Carbon dioxide decomposition through gas exchange in barium calcium iron niobates

Kildahl, Harriet; Li, Zhongbo; Cao, Hui; Slater, Peter; Ding, Yulong

DOI:

[10.1016/j.cattod.2020.05.024](https://doi.org/10.1016/j.cattod.2020.05.024)

License:

Creative Commons: Attribution-NonCommercial-NoDerivs (CC BY-NC-ND)

Document Version

Peer reviewed version

Citation for published version (Harvard):

Kildahl, H, Li, Z, Cao, H, Slater, P & Ding, Y 2020, 'Carbon dioxide decomposition through gas exchange in barium calcium iron niobates', *Catalysis Today*. <https://doi.org/10.1016/j.cattod.2020.05.024>

[Link to publication on Research at Birmingham portal](#)

General rights

Unless a licence is specified above, all rights (including copyright and moral rights) in this document are retained by the authors and/or the copyright holders. The express permission of the copyright holder must be obtained for any use of this material other than for purposes permitted by law.

- Users may freely distribute the URL that is used to identify this publication.
- Users may download and/or print one copy of the publication from the University of Birmingham research portal for the purpose of private study or non-commercial research.
- User may use extracts from the document in line with the concept of 'fair dealing' under the Copyright, Designs and Patents Act 1988 (?)
- Users may not further distribute the material nor use it for the purposes of commercial gain.

Where a licence is displayed above, please note the terms and conditions of the licence govern your use of this document.

When citing, please reference the published version.

Take down policy

While the University of Birmingham exercises care and attention in making items available there are rare occasions when an item has been uploaded in error or has been deemed to be commercially or otherwise sensitive.

If you believe that this is the case for this document, please contact UBIRA@lists.bham.ac.uk providing details and we will remove access to the work immediately and investigate.

Carbon Dioxide Decomposition Through Gas Exchange in Barium Calcium Iron Niobates

Harriet Kildahl^{*a}, Zhongbo Li^{*b}, Hui Cao^{a, †}, Peter Slater^c, Yulong Ding^a

^a School of Chemical Engineering, University of Birmingham, Birmingham, United Kingdom

^b Beijing District Heating Group, China

^c School of Chemistry, University of Birmingham, Birmingham, United Kingdom

[†] Corresponding author: h.cao@bham.ac.uk

*Both authors contributed equally to this manuscript

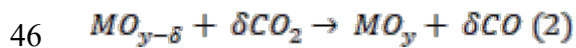
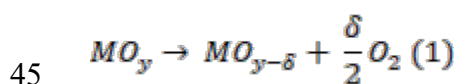
Abstract

A number of metal oxides and perovskites are capable of being reduced at high temperatures and then re-oxidised in the presence of CO₂ or H₂O to form CO or H₂. Barium calcium iron niobates have been found to be redox-active in this way. The redox activity of these perovskites was explored, and the chemical and physical stability was investigated using EDX and SEM imaging, respectively. The most promising, Ba₂Ca_{0.66}Nb_{0.34}FeO_{6-δ} (BCNF1), showed mass changes of 0.45% after five cycles of reduction with N₂ and re-oxidation with 10% CO₂. BCNF1 is chemically stable as it shows no changes in XRD and shows no evidence of sintering, although cracking of the pellets was observed after re-oxidation. The low enthalpy of re-oxidation of BCNF1 coupled with the high and sustained mass change makes this perovskite suitable for chemical looping use for energy storage and conversion systems.

Keywords: Carbon dioxide conversion, perovskite, CO₂ reduction, chemical looping, barium calcium iron niobates

24 1. Introduction

25 With the shift towards a 100% renewable future well underway, there are still areas where
26 gains in efficiency and decreases in losses can be made. One of these areas is industrial waste
27 heat. There are many industries which require heat such as chemical, food and drink, textiles
28 and metal processing. The 28 members of the European Union required 1820 TWh of energy
29 as heat across all industries in 2018, which amounts to around 70% of total energy
30 consumption by industry[1]. More than 48% of this heat is over 500 °C with up to 28% hotter
31 than 1000 °C. The iron and steel industries are particularly attractive for waste heat recovery
32 or usage since the temperatures can be up to 2000 °C[2]. Industrial-scale demonstrations have
33 been built to store the waste heat in thermal energy and later on reuse it for
34 industrial/domestic heating[3]. A recently proposed novel concept of exploiting this waste
35 heat is to use a thermochemical cycle where changes in temperature are used to decompose
36 small molecules such as CO₂ or H₂O into CO and H₂[4]. Carbon monoxide and hydrogen can
37 be used as syngas for the Fischer-Tropsch process, to produce essential chemicals without the
38 need for crude oil[5], or as a fuel in a fuel cell device. The iron and steel industries also have
39 high CO₂ emissions, such as 1.22 tonnes of CO₂ per tonne of product produced in a blast
40 furnace[6]. Therefore, both heat and increased CO₂ concentrations could be found in these
41 industries, which would be ideal for the implementation of a thermochemical material and
42 help to reduce direct emissions. CO production from carbon dioxide by a thermochemical
43 cycle was found to be more than 2.5 times more efficient than algae-based biomass
44 conversions when using waste heat from industry[7].



47 A thermochemical cycle works through the addition of heat, causing reduction of the
48 material. Oxygen is released from the material resulting in the formation of oxygen vacancies
49 throughout the structure (Equation 1). Upon the addition of CO₂ or H₂O, the material is re-
50 oxidised, often at a lower temperature, and the oxygen vacancies are filled while CO or H₂ is
51 released (Equation 2). As can be seen from Equation (1) and (2), fuel production is increased
52 with an increase in the oxygen non-stoichiometry, δ . Therefore, the efficiency and fuel
53 production yield can be increased by aiding the diffusion of gases throughout the material. If
54 oxygen is lost throughout the material rather than only the surface, more oxygen vacancies

55 can be formed. This greater level of reduction leads to deeper oxidation as there are more
56 oxygen vacancies to be filled. This leads to a greater decomposition of CO₂ or H₂O and
57 therefore greater fuel production. The diffusion of gases within the material can be aided by
58 increases in porosity or surface area to volume ratio.

59 The two main classes of materials capable of undergoing a thermochemical cycle are simple
60 metal oxides or mixed metal oxides, such as perovskites. Of the simple metal oxides, the
61 most researched is ceria (cerium oxide) which can split both carbon dioxide and water with
62 good yields; however, it requires high temperatures such as 1400 °C for reduction and 900 °C
63 for oxidation[8]. Ceria is a non-stoichiometric oxygen carrier meaning that less than one mole
64 of oxygen is released per mole of ceria. Other metal oxides include the volatile metal oxides
65 and iron oxides. Volatile metal oxides are stoichiometric oxygen carriers and have melting
66 temperatures of the pure metal lower than the reduction temperature of the metal oxide. For
67 example, ZnO has a reduction temperature of 2000 °C but a melting temperature of 420 °C,
68 meaning that the gaseous zinc must be quenched quickly to avoid recombination with
69 oxygen[9]. Pure iron oxide (Fe₃O₄) can be reduced at 2200 °C; however, it can be oxidised
70 easily by water at 175 °C[10].

71 Perovskites are non-stoichiometric mixed metal oxides with an ideal formula of ABO₃. The
72 most researched perovskite for thermochemical cycles is the La_{1-x}Sr_xMnO₃ family, which can
73 be reduced at about 1400 °C and oxidised at around 900 °C with up to ten times higher fuel
74 yields than ceria[11]. Ba₂Ca_{0.66}Nb_{1.34-x}Fe_xO₆ (x = 0, 0.34, 0.66 and 1) is a double perovskite-
75 type and can be reduced and made to decompose CO₂ at 700 °C[12]. This paper will
76 investigate the barium calcium iron niobate perovskite family for their ability to split carbon
77 dioxide at 700 °C. The redox activity of these materials will be measured predominantly by
78 mass change during the thermochemical cycles along with tracking of changes to the crystal
79 structure and surface morphology during the reaction.

80 **2. Experiment**

81 **2.1 Material Synthesis**

82 Ba₂Ca_{0.66}Nb_{1.34-x}Fe_xO₆ perovskites were synthesised through a solid-state reaction as
83 performed previously[12]. Four perovskites were synthesised by varying the concentrations
84 of niobium and iron in the B-site while maintaining the concentration of calcium in the B-site
85 and barium in the A-site. The four perovskites tested are Ba₂Ca_{0.66}Nb_{1.34}O_{6-δ} (x = 0, named
86 BCNF0), Ba₂Ca_{0.66}NbFe_{0.34}O_{6-δ} (x = 0.34, named BCNF0.34), Ba₂Ca_{0.66}Nb_{0.68}Fe_{0.66}O_{6-δ} (x =

87 0.66, named BCNF0.66) and $\text{Ba}_2\text{Ca}_{0.66}\text{Nb}_{0.34}\text{FeO}_{6-\delta}$ ($x = 1$, named BCNF1). Stoichiometric
88 ratios of the precursors (BaCO_3 (Alfa Aesar, 99%), CaCO_3 (Alfa Aesar, 99.5%), Nb_2O_5 (Alfa
89 Aesar, 99.5%), Fe_2O_3 (J.T.Baker, 99%)) were mixed in a ball mill (Fritsch Pulverisette) at
90 350 rpm for 30 minutes. The resulting powder was calcined in air at 1000 °C for 12 hours
91 (Carbolite, HTF18/27) before ball milling again. The powder was pressed into 13mm
92 diameter pellets with isostatic pressure of 120 MPa (Lloyd Instruments, LS100Plus) and
93 sintered at 1400 °C for 24 hours.

94 2.2 Material Characterisation

95 X-ray diffraction (XRD) was performed on a Bruker d8 Advance X-ray Diffractometer with
96 $\text{Cu K}\alpha$ radiation ($\lambda=1.54 \text{ \AA}$) over the 2θ range between 10° and 80° with a step size of 0.02°
97 and 3 seconds per step. The pellets were measured whole. Lattice parameters were calculated
98 by solving the least-squares of 2θ , using Bragg's Law and the plane spacing equation.
99 Scanning electron microscopy (SEM) (Hitachi TM3030) with energy dispersive X-ray (EDX)
100 was used to investigate the surface structure of the pellets and the composition of the surface
101 layers. Helium Pycnometry (Accupyc II 1340) was used to determine the density and porosity
102 of the perovskite pellets. Microcomputer tomography (Micro CT) (Bruker SkyScan 2211)
103 was used to visualise the 3D structure of the pellets to investigate gas exchange.

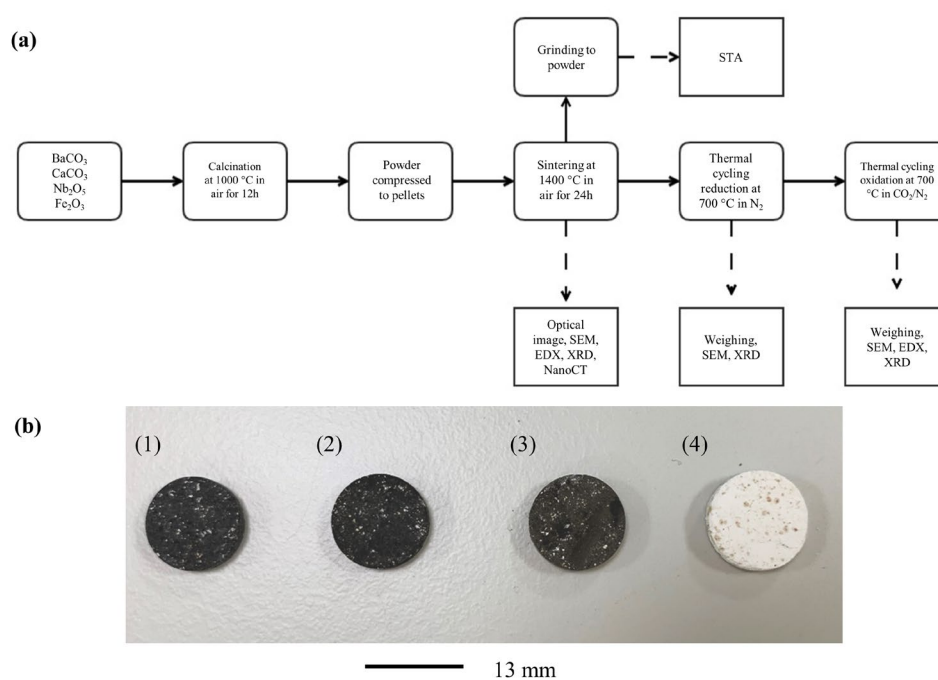
104 2.3 Thermal Cycle of Perovskites

105 The perovskites were tested for catalytic ability in a tubular furnace with controlled gas flows
106 (Elite Thermal Systems Ltd TSH15/50/450). The pellets were inserted into the furnace, and
107 the furnace was heated to 700 °C with a nitrogen flow of 50 ml/min. The pellets were
108 reduced for 24 hours before being weighed and characterised with SEM, EDX and XRD. The
109 pellets were heated again to 700 °C with a 10% CO_2 /90% N_2 flow of 50 ml/min and left to
110 react for 24 hours. The pellets were weighed again, and characterisation with SEM, EDX and
111 XRD was repeated. Simultaneous thermal analysis (Linseis STA PT1600/800) was used to
112 calculate the enthalpy of the CO_2 reaction. The experimental flowchart is shown in Figure 1
113 (a). Thermal cycling was performed by alternating 24 hours of reduction under nitrogen at 700
114 °C with 24 hours of oxidation under 10 % CO_2 / 90 % N_2 at 700 °C for five cycles. After
115 each step of the cycle, the pellets were cooled to room temperature and weighed.

116 3. Results and Discussion

117 3.1 Material Characterisation

118 Characterisation of the as-prepared perovskites was undertaken to confirm their phase
 119 formation. The as-prepared pellets can be seen in Figure 1(b). The iron-containing
 120 perovskites (BCNF1 (1), BCNF0.66 (2) and BCNF0.34 (3)) are black while BCNF0 (4)
 121 which contains no iron is white. Helium pycnometry (Table 1) shows an increase in density
 122 with increasing niobium content due to the higher molecular weight of niobium compared to
 123 iron. Porosity also generally increases with increasing niobium content, and it can be seen in
 124 Figure 1(b) that the BCNF0 pellets are slightly larger than the iron-containing pellets
 125 (BCNF0.34, BCNF0.66 and BCNF1), despite being made in the same mould, indicating less
 126 shrinkage on sintering. This correlates with the much higher pore volume in BCNF0. This is
 127 in agreement with the literature where doping with larger atomic radii elements results in
 128 greater porosity[13].



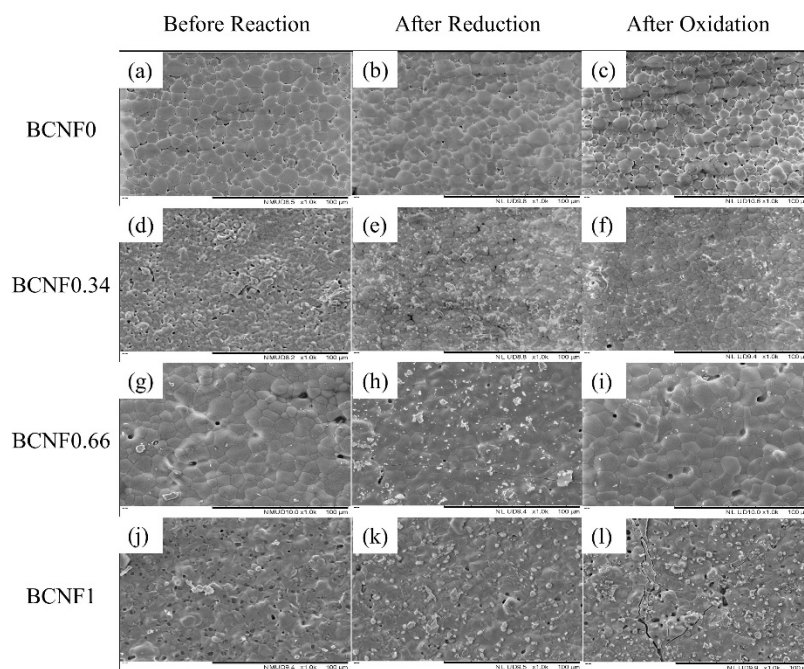
129
 130 Figure 1. (a) Experimental workflow, (b) Visual representation of the as-synthesized pellets, (1) BCNF1, (2) BCNF0.66, (3)
 131 BCNF0.34 and (4) BCNF0

132 Table 1. Helium pycnometry results showing density, pore volume and porosity

Sample	Mass (g)	Density (g/cm ³)	Pore volume (cm ³ /g)	Porosity (%)
BCNF1	0.472	6.1003	0.1687	50.70
BCNF0.66	0.462	6.2382	0.2512	61.04
BCNF0.34	0.468	6.3966	0.2278	59.31
BCNF0	0.441	6.6309	0.3231	68.18

133
 134 SEM images with x1000 magnification of the as-prepared perovskites can be seen in Figure
 135 2. The as-prepared BCNF0 perovskite without iron (a) had an average grain size around

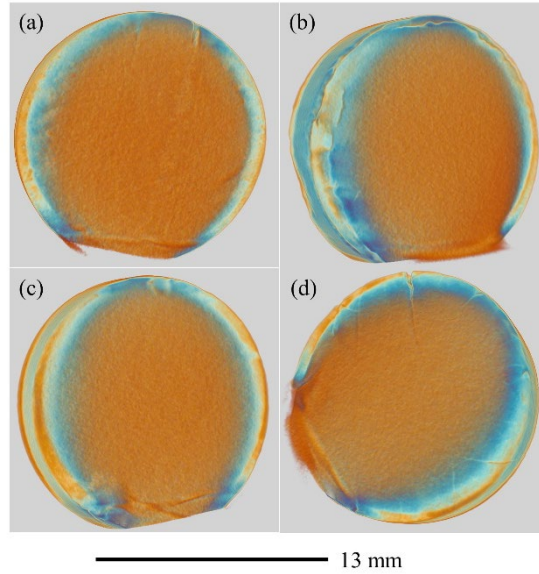
136 10 μ m with no grains larger than 20 μ m and pores of around 1 μ m. BCNF0 had the smallest
 137 variation in grain sizes of any of the perovskites. The BCNF0.34 perovskite (d) had an
 138 average grain size below 5 μ m with a high density of pores. The as-prepared BCNF0.66
 139 perovskite (g) had larger grains than BCNF0 or BCNF0.34 with an average size of around
 140 20 μ m and a few large pores around 8 μ m. The grain sizes in the as-prepared BCNF1 (j), the
 141 perovskite with the most iron, are not distinguishable.



142

143 *Figure 2. SEM images of as-prepared, after reduction and after re-oxidation of the four perovskites, BCNF0, BCNF0.34,*
 144 *BCNF0.66 and BCNF1*

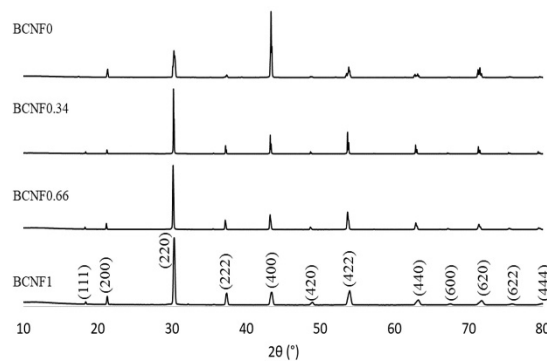
145 The Micro CT scans (Figure 3) of the four perovskites reveal that the core of the pellets has a
 146 higher density than the outer edges of the pellets, which likely occurred during the high-
 147 pressure moulding of the pellets. Additionally, the faces of the pellets are textured rather than
 148 smooth, showing that the surface is porous, as was seen in the SEM images and confirmed by
 149 helium pycnometry.



150

151 *Figure 3. Micro Computer Tomography Reconstructed Images of (a) BCNF0, (b) BCNF0.34, (c) BCNF0.66, and (d)*
 152 *BCNF1.*

153 XRD data of the as-prepared perovskites (Figure 4) shows that all perovskites had a double-
 154 perovskite type face centred cubic structure with an $Fm\bar{3}m$ space group. The average lattice
 155 parameters and miller indexing can be seen in Table 2. The perovskites synthesised here
 156 showed similar XRD patterns and crystal structures as other Barium Calcium Iron Niobates
 157 synthesised in the literature[12,14,15], with some variations in relative intensities of peaks,
 158 which may relate to some preferred orientation of the crystallites within the pellets. None of
 159 the impurities seen in the literature of these compounds could be identified here, including
 160 $BaCO_3$, Fe_2C , C and Fe_3O_4 [15], supporting the purity of the samples in the present study.



161

162 *Figure 4. X-ray diffraction patterns of as-synthesized BCNF1, BCNF0.66, BCNF0.34 and BCNF0.*

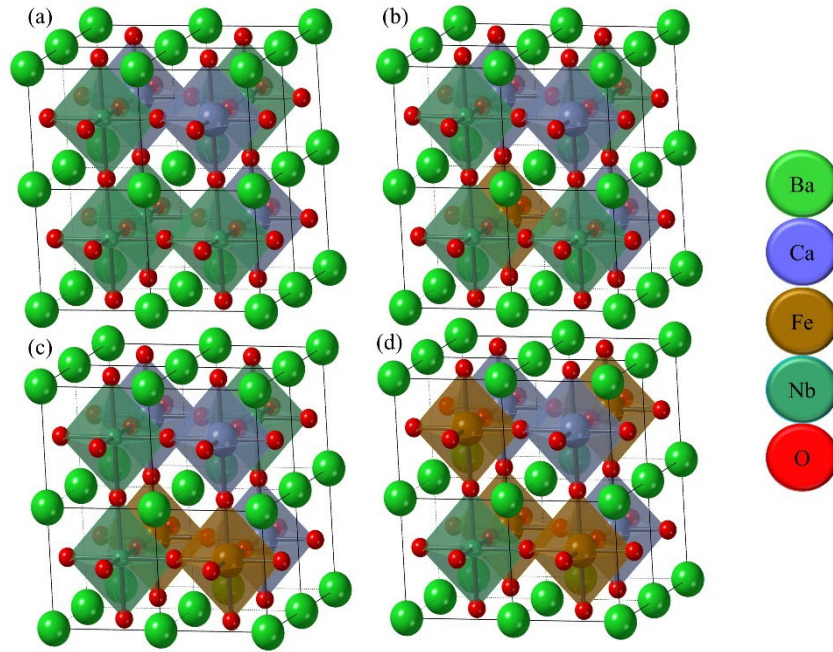
163 *Table 2. Indexed XRD data for BCNF1, BCNF0.66, BCNF0.34 and BCNF0 with d spacing and intensity*

			BCNF1		BCNF0.66		BCNF0.34		BCNF0	
h	k	l	d(Å)	I(%)	d(Å)	I(%)	d(Å)	I(%)	d(Å)	I(%)

1	1	1	4.831	7	4.852	5	4.831	4	5.089	2
2	0	0	4.174	15	4.198	11	4.182	6	4.166	13
2	2	0	2.950	100	2.962	100	2.958	100	2.952	41
2	2	2	2.404	19	2.417	16	2.414	13	2.404	5
4	0	0	2.081	21	2.092	24	2.091	29	2.086	100
4	2	0	1.861	6	1.870	5	1.869	4	1.862	2
4	2	2	1.699	23	1.706	28	1.706	34	1.702	17
4	4	0	1.470	10	1.477	11	1.478	14	1.472	6
6	0	0	1.385	4	1.392	3	1.393	2	1.388	2
6	2	0	1.314	8	1.321	9	1.319	6	1.318	16
6	2	2	1.253	4	1.259	5	1.260	2	1.258	2
4	4	4	1.201	4	1.205	4	1.207	4	1.203	2
			a = 8.344Å		a = 8.377Å		a = 8.366Å		a = 8.345Å	

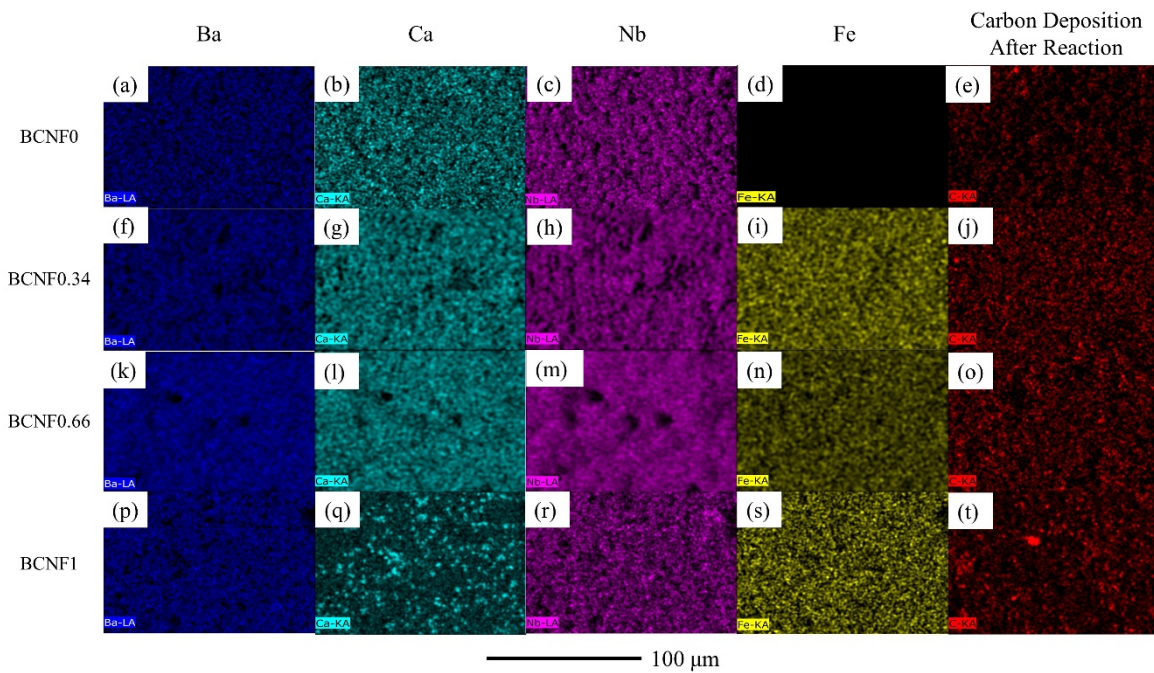
164

165 The double-perovskite type crystal structures can be seen in Figure 5, with calcium, niobium
166 and iron occupying the B-sites and barium occupying the A-sites. The EDX scans in Figure 6
167 of as-prepared BCNF0, BCNF0.34 and BCNF0.66 show an even distribution of all elements,
168 which suggests a uniform sample. On the other hand, BCNF1 shows small clumps of calcium
169 with many areas containing no calcium at all. Since XRD analysis shows that the correct
170 perovskite was synthesized, it can be suggested that the calcium seen in lumps on the surface
171 of the perovskite does not represent the spread of elements within the whole pellet. There are
172 many small patches of around 4µm on the surface, which through EDX analysis are seen to
173 contain high concentrations of calcium. The CaCO₃ starting material had a powder size less
174 than 5µm and so these patches are highly likely to be unreacted CaCO₃ starting material.



175

176 *Figure 5. Crystal Structures of (a) BCNF0, (b) BCNF0.34, (c) BCNF0.66 and (d) BCNF1*



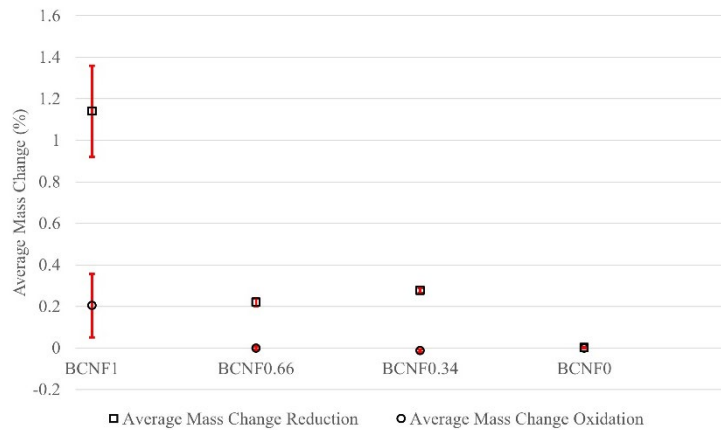
177

178 *Figure 6. EDX Scans of as-synthesized BCNF1, BCNF0.66, BCNF0.34 and BCNF0*

179 **3.2 Reduction and Oxidation**

180 The average mass change during reduction and re-oxidation of the perovskites in the tubular
 181 furnace at 700 °C can be seen in Figure 7, and error bars showing one standard deviation are
 182 shown in red. Firstly, BCNF0 showed no mass change during reduction or re-oxidation,
 183 supporting that iron is needed in the barium calcium iron niobates. This finding has also been
 184 confirmed in the literature[12]. BCNF0.34 and BCNF0.66 lost 0.28 and 0.21 % mass during

185 reduction respectively; however, both showed no mass gain during re-oxidation. In fact,
186 BCNF0.34 showed a minimal amount of mass loss during re-oxidation, perhaps since
187 nitrogen was used during the reduction step and 90 % nitrogen with 10 % carbon dioxide was
188 used during re-oxidation. This could suggest that a higher concentration of carbon dioxide is
189 necessary for the re-oxidation of BCNF0.34 and BCNF0.66. The 10% carbon dioxide
190 mixture used for re-oxidation was chosen to mimic flue gases from iron and steel processing
191 industries. BCNF1 showed the highest mass loss during reduction, 1.14 %. This high level of
192 reduction suggests that oxygen vacancies are forming easily, likely due to the high iron
193 content, allowing more oxygen vacancies to form. Re-oxidation of BCNF1 with 10 % carbon
194 dioxide resulted in a 0.2 % increase in mass. It is common that perovskites are not completely
195 re-oxidised during the re-oxidation reaction [16–19]. This suggests that not all oxygen
196 vacancies formed during reduction are filled during the re-oxidation step. This could be due
197 to the low carbon dioxide content (10 %) which could mean that carbon dioxide was not
198 coming into contact with the oxygen vacancies in the material. Secondly, the low extent of
199 re-oxidation could be due to the high density of the pellets, as seen in the Micro CT images in
200 Figure 3, particularly in the core of the pellet, meaning that gas exchange was likely not
201 possible within the pellet but rather just on the surface. **Reactivity of the four perovskites had
202 an inverse relationship with porosity, suggesting that gas exchange was not the limiting factor
203 but rather the material itself, particularly in the case of BCNF0. It is likely that increasing the
204 porosity of BCNF1 would increase its reactivity; this will be investigated in future research.**
205 It must be noted that the position in the tubular furnace is not linked to the extent of reduction
206 or oxidation for any of the perovskites.



207

208 *Figure 7. Average Mass Change of the Four Perovskites During Reduction and Re-oxidation*

209 The difference in the reactivities of the four perovskites can be partially explained by the
 210 enthalpy of oxidation calculated from STA measurements (Table 3). A negative enthalpy of
 211 oxidation suggests an exothermic reaction which a positive enthalpy suggests an endothermic
 212 reaction. The enthalpy of the oxidation reaction for BCNF1 is -45 J/g, which is very small
 213 compared to the energy required to raise the perovskite to the reaction temperature of 700 °C,
 214 which is around 2570 J/g. This energy likely incorporates the enthalpy of reduction and the
 215 energy required to heat the perovskite. This energy requirement is likely much higher for
 216 BCNF1 because it contains more iron and can therefore form more oxygen vacancies. Part of
 217 this large enthalpy could be rearrangement within the crystal structure to allow oxygen to
 218 move from within the material to the surface of the material. This would allow more oxygen
 219 to be released during the reduction step; this was observed in the experimental studies. In
 220 order to elucidate the effect reduction is playing on the magnitude of this energy, future
 221 research using STA will maintain the perovskite at 700 °C while cycling between nitrogen
 222 and carbon dioxide atmospheres in order to separate the enthalpy of reduction. However, the
 223 low enthalpy of re-oxidation of BCNF1 means that when the perovskite is kept at 700 °C, the
 224 energy required to cycle between the oxidation and reduction reactions is very small, which
 225 should lead to a high level of energy storage with very little energy lost to the reaction. Since
 226 the enthalpy of oxidation for BCNF1 is exothermic, this suggests that the products (the
 227 oxidised perovskite and carbon) are more stable than the reactants (the reduces perovskite
 228 with oxygen vacancies and carbon dioxide) and therefore the oxidation reaction is
 229 energetically favourable. However, the enthalpy of oxidation for BCNF0.66 and BCNF0.34
 230 are only around -1J/g, likely the difference in stability is not large enough to make the
 231 reaction favourable. BCNF0 has an endothermic reaction enthalpy, meaning the products are

232 less stable than the reactants and therefore the reaction is less favourable. The enthalpy
233 results also explain the fact that compounds similar to BCNF0 are unable to split carbon
234 dioxide in the literature[12,14,15,20–23].

235 *Table 3. Enthalpy calculations of the four perovskites calculated from simultaneous thermal analysis.*

Perovskite	Energy to heat from 25 to 750 °C (J/g)	Enthalpy of oxidation (J/g)
BCNF1	2570.89	-45.11
BCNF0.66	2046.13	-1.04
BCNF0.34	1337.06	-1.11
BCNF0	458.85	0.14

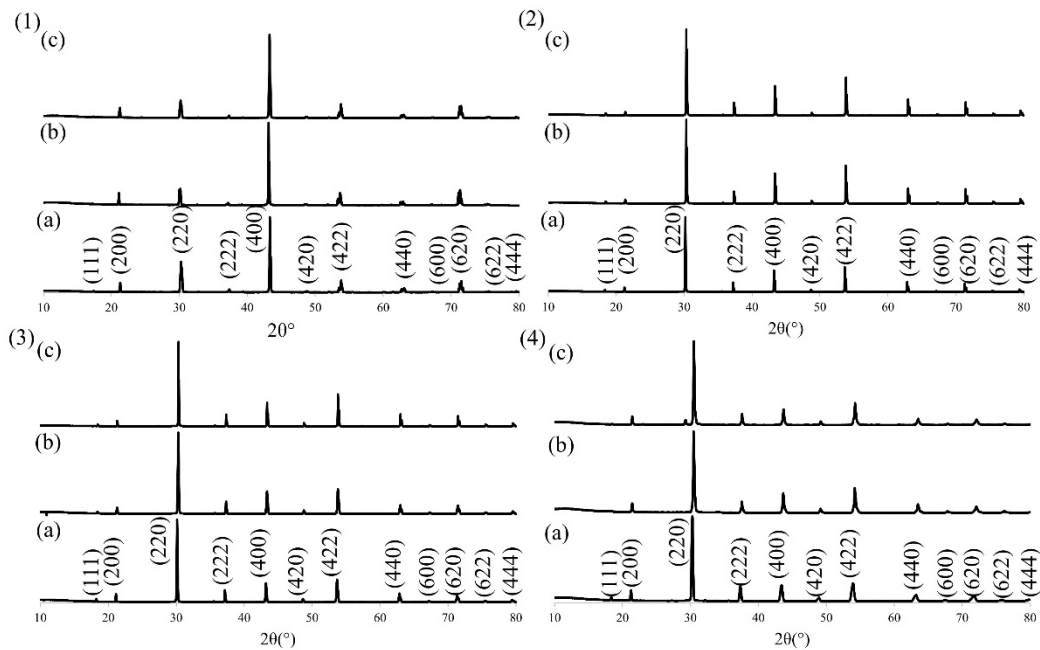
236

237 EDX analysis (Figure 6) of the pellets after oxidation in 10% CO₂ were used to visualise
238 carbon deposition on the surface of the pellets. BCNF0 (e) clearly shows the least carbon
239 deposition on its surface compared to the other three perovskites. This small amount of
240 carbon on the surface could be due to the carbonate salts used in the synthesis of the
241 perovskite, suggesting that the carbonate was not completely reacted during calcining and
242 sintering. Moving from BCNF0.33 (j) to BCNF0.66 (o) and BCNF1 (t) there is an increase in
243 the size of the carbon deposition particles, with large patches forming in BCNF1. Given that
244 there was no mass gain during re-oxidation for BCNF0.34 and BCNF0.66, this carbon
245 deposition could again be due to improper removal of carbonate salts during synthesis or very
246 minimal surface deposition. The large clumps of carbon deposition on BCNF1 are not likely
247 to be from the carbonate salts since it does not present this way in any other perovskite. This
248 suggests that some of the CO₂ has been split into carbon on the surface of BCNF1, showing
249 the high activity of this phase for CO₂ reduction.

250 **3.3 Perovskite stability**

251 XRD scans (Figure 9) of the perovskites as-prepared, after reduction and after re-oxidation
252 were taken to investigate the chemical stability of the perovskites throughout the cycle. For
253 BCNF0 (1), it can be seen that there were very little changes throughout the cycle, as
254 expected from the lack of redox activity in this material. BCNF0.34 (2), BCNF0.66 (3) and
255 BCNF1 (4) also showed no change in XRD pattern throughout the cycle showing that they
256 are stable at 700 °C and under a 10 % CO₂ flow. In agreement with previous research, the
257 BCNF1 perovskite did not show evidence of carbon deposition after re-oxidation (4c),
258 usually visible as a small peak after the (422) reflection at around 55° [15]. In previous

259 research, this carbon peak was only seen after re-oxidation with pure CO₂ while the reaction
 260 with 2000ppm CO₂ did not show a carbon peak.



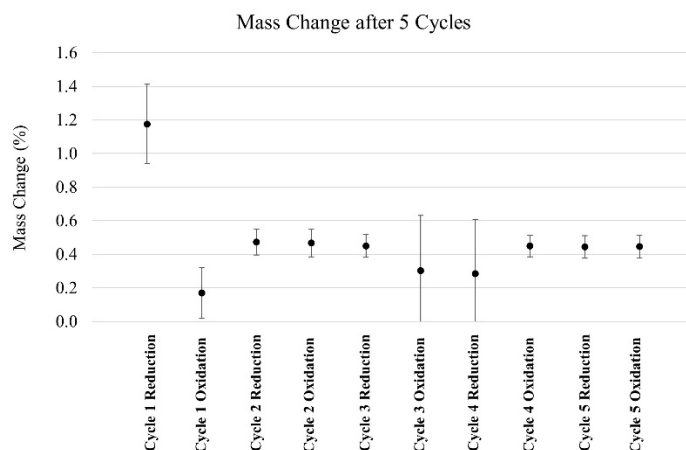
261

262 *Figure 8. XRD Scans of (1) BCNF0, (2) BCNF0.34, (3) BCNF0.66 and (4) BCNF1 with (a) as-prepared, (b) after reduction*
 263 *and (c) after re-oxidation*

264 SEM images (Figure 2) were taken of the as-prepared perovskites, after reduction and after
 265 re-oxidation to assess the structural stability of the perovskites. In BCNF0, after reduction
 266 (1b) the average grain size had decreased from around 10 μ m to less than 10 μ m and fewer
 267 pores were visible. There was also less definition between the grain boundaries. After re-
 268 oxidation (1c) the definition of the grain boundaries has increased, the grain size has grown to
 269 larger than 10 μ m, and there are more pores visible, most around 3 μ m. This suggests that
 270 sintering has occurred due to the increase in grain size. In BCNF0.34 after reduction (2b), the
 271 average pore size had increased from less than 5 μ m to around 10 μ m, and fewer pores are
 272 present, suggesting sintering has occurred. Additionally, there is a small amount of deposition
 273 on the surface which appears to have a high concentration of calcium through EDX analysis
 274 (Figure 6 (g)). After re-oxidation (2c), there are markedly fewer pores and less deposition on
 275 the surface, suggesting the calcium-containing deposits were reacted or incorporated into the
 276 structure. The average grain size remains unchanged through the re-oxidation step. The as-
 277 prepared BCNF0.66 (3a) perovskite had larger grains than BCNF0 or BCNF0.34. After
 278 reduction (3b), the grain boundaries are less pronounced, and the pore sizes have decreased
 279 from around 8 μ m to just a few microns. Overall, the grains are roughly the same size as the
 280 as-prepared sample; however, there is again some solid deposition. After re-oxidation (3c),

281 there is an increase in grain size, with some of the larger grains above 30 μ m and an increase
282 in the number and size of pores. There is also a significant decrease in deposition on the
283 surface, as seen in BCNF0.34 after re-oxidation. After reduction of BCNF1 (4b), the
284 perovskite again has indistinguishable grain sizes, a few pores and deposition on the surface.
285 After re-oxidation (4c), a large crack can be seen running the length of the scanned area and
286 upon visual observation, many large cracks had appeared over the surface of the pellet. The
287 cracking of the pellet suggests significant volume changes during the redox process;
288 however, the cracks may help gas diffusion and penetration in later cycles.

289 Figure 9 shows the mass change observed through five cycles of reduction in 100% N₂ and
290 re-oxidation in 10% CO₂/90% N₂ for BCNF1. It can be seen that although the mass gain in
291 the first re-oxidation cycle was only 0.2 %, from the second cycle, the mass changes stabilise
292 at around 0.45 %. This increase in the reactivity of the CO₂ splitting reaction between the first
293 and second cycle is likely due to morphological changes since no changes were seen in the
294 XRD after the first cycle. Figure 2 shows that the pellet had cracks on the surface after the
295 first cycle, which could have led to a larger surface area for the reaction to occur, resulting in
296 a larger mass change in the second cycle. The lower mass change for the 3rd re-oxidation and
297 4th reduction is accompanied by a much higher standard deviation between the pellets,
298 perhaps suggesting some human or mechanical error during weighing. This is likely the case
299 because the mass change returns to 0.45% after these two points, making error more likely.
300 However, the sustained mass change of 0.45 % is extremely promising in terms of potential
301 applications of this material. This mass change can be converted to oxygen evolution and
302 carbon monoxide production volumes, giving an average over five cycles of 140 μ mol of O₂
303 per gram of perovskite and 160 μ mol of CO per gram. This fuel yield is higher than many
304 ceria-based materials[8].



305

306 *Figure 9. Mass change of BCNF1 during five cycles of reduction and re-oxidation*

307 **4. Conclusion**

308 The results presented here show that for the barium calcium iron niobate family of
 309 perovskites, the higher the iron content, the more successful for chemical looping and the
 310 decomposition of carbon dioxide. BCNF1, $\text{Ba}_2\text{Ca}_{0.66}\text{Nb}_{0.34}\text{FeO}_{6-\delta}$, showed an exceptionally
 311 high mass loss during reduction of 1.14%, equal to the loss of 0.34 moles of oxygen. The
 312 sustained mass change of 0.45 % after five cycles suggests this material could be suitable for
 313 use in chemical looping energy storage applications. More importantly, the low enthalpy
 314 change of oxidation of BCNF1 suggests that very little energy would be lost cycling the
 315 material, meaning more of the energy input can be regained.

316 **Acknowledgements**

317 The authors would like to thank the University of Birmingham and UK EPSRC and
 318 acknowledge financial support from UK EPSRC under EP/S016627/1 and EP/R024006/1.

319 **References**

- 320 [1] G. Kosmadakis, Estimating the potential of industrial (high-temperature) heat pumps for
 321 exploiting waste heat in EU industries, *Appl. Therm. Eng.* 156 (2019) 287–298.
- 322 [2] R.C. McKenna, J.B. Norman, Spatial modelling of industrial heat loads and recovery
 323 potentials in the UK, *Energy Policy*. 38 (2010) 5878–5891.
- 324 [3] H. Fang, J. Xia, K. Zhu, Y. Su, Y. Jiang, Industrial waste heat utilization for low temperature
 325 district heating, *Energy Policy*. 62 (2013) 236–246.
- 326 [4] Y. Ding, H. Cao, P. Slater, Y. Li, S. Du, *Energy Generation*, WO/2019/158948, 2019.
- 327 [5] D. Marxer, P. Furler, J. Scheffe, H. Geerlings, C. Falter, V. Batteiger, A. Sizmann, A.
 328 Steinfeld, Demonstration of the Entire Production Chain to Renewable Kerosene via Solar
 329 Thermochemical Splitting of H_2O and CO_2 , *Energy and Fuels*. 29 (2015) 3241–3250.

- 330 [6] N. Pardo, J.A. Moya, Prospective scenarios on energy efficiency and CO₂ emissions in the
331 European Iron & Steel industry, *Energy*. 54 (2013) 113–128.
- 332 [7] D.S. Mallapragada, N.R. Singh, V. Curteanu, R. Agrawal, Sun-to-fuel assessment of routes for
333 fixing CO₂ as liquid fuel, *Ind. Eng. Chem. Res.* 52 (2013) 5136–5144.
- 334 [8] R.R. Bhosale, G. Takalkar, P. Sutar, A. Kumar, F. AlMomani, M. Khraisheh, A decade of
335 ceria based solar thermochemical H₂O/CO₂ splitting cycle, *Int. J. Hydrogen Energy*. In Press
336 (2018) 1–27.
- 337 [9] A. Steinfeld, Solar hydrogen production via a two-step water-splitting thermochemical cycle
338 based on Zn/ZnO redox reactions, *Int. J. Hydrogen Energy*. 27 (2002) 611–619.
- 339 [10] T. Kodama, N. Gokon, Thermochemical cycles for high-temperature solar hydrogen
340 production, *Chem. Rev.* 107 (2007) 4048–4077.
- 341 [11] J.R. Scheffe, D. Weibel, A. Steinfeld, Lanthanum-strontium-manganese perovskites as redox
342 materials for solar thermochemical splitting of H₂O and CO₂, *Energy and Fuels*. 27 (2013)
343 4250–4257. <https://doi.org/10.1021/ef301923h>.
- 344 [12] S. Mulmi, H. Chen, A. Hassan, J.F. Marco, F.J. Berry, F. Sharif, P.R. Slater, E.P.L. Roberts, S.
345 Adams, V. Thangadurai, Thermochemical CO₂ splitting using double perovskite-type
346 Ba₂Ca_{0.66}Nb_{1.34-x}Fe_xO_{6-δ}, *J. Mater. Chem. A*. 5 (2017) 6874–6883.
- 347 [13] T. Tsuji, Y. Ohashi, Y. Yamamura, Effect of ionic radius on electrical conductivity of doped
348 SmAlO₃ perovskite oxide, *Solid State Ionics*. (2002).
- 349 [14] S. Mulmi, V. Thangadurai, Preparation, Structure and CO₂ Sensor Studies of BaCa_{0.33}Nb_{0.67-}
350 _xFe_xO_{3-δ}, *J. Electrochem. Soc.* 160 (2013) B95–B101.
- 351 [15] S. Mulmi, *Greenhouse Gas Detection Using Metal Oxides: Experiments and Challenges*, 2016.
- 352 [16] R.D. Barcellos, M.D. Sanders, J. Tong, A.H. McDaniel, R.P. O’Hayre, BaCe_{0.25}Mn_{0.75}O_{3-δ}
353 promising perovskite-type oxide for solar thermochemical hydrogen production, *Energy*
354 *Environ. Sci.* 11 (2018) 3256–3265.
- 355 [17] A.E. Ramos, D. Maiti, Y.A. Daza, J.N. Kuhn, V.R. Bhethanabotla, Co, Fe, and Mn in La-
356 perovskite oxides for low temperature thermochemical CO₂ conversion, *Catal. Today*. 338
357 (2019) 52–59.
- 358 [18] B.J. Hare, D. Maiti, S. Ramani, A.E. Ramos, V.R. Bhethanabotla, J.N. Kuhn, Thermochemical
359 conversion of carbon dioxide by reverse water-gas shift chemical looping using supported
360 perovskite oxides, *Catal. Today*. 323 (2018) 225–232.
- 361 [19] L. Wang, M. Al-Mamun, P. Liu, Y.L. Zhong, Y. Wang, H.G. Yang, H. Zhao, Enhanced
362 Thermochemical H₂ Production on Ca-Doped Lanthanum Manganite Perovskites Through
363 Optimizing the Dopant Level and Re-oxidation Temperature, *Acta Metall. Sin. English Lett.*
364 31 (2018) 431–439.
- 365 [20] S. Mulmi, A. Hassan, P. Pereira-Almao, V. Thangadurai, Detecting CO₂ at ppm level in
366 synthetic air using mixed conducting double perovskite-type metal oxides, *Sensors Actuators*
367 *B Chem.* 178 (2013) 598–605.
- 368 [21] S. Mulmi, R. Kannan, V. Thangadurai, CO₂ and SO₂ tolerant Fe-doped metal oxides for solid
369 state gas sensors, *Solid State Ionics*. 262 (2014) 274–278.
- 370 [22] S. Mulmi, R. Kannan, V. Thangadurai, Mixed Ion and Electron Conducting Ceramics for Gas
371 Sensors, *ECS Trans.* 58 (2014) 31–36.
- 372 [23] R. Kannan, S. Mulmi, V. Thangadurai, Synthesis and characterization of perovskite-type
373 BaMg_{0.33}Nb_{0.67-x}Fe_xO_{3-δ} for potential high temperature CO₂ sensors application, *J. Mater.*

